Supporting Information - Photoinhibition of FeFe hydrogenase

Matteo Sensi,[†,▽] Carole Baffert,[†] Laura Fradale,[†] Charles Gauquelin,[‖] Philippe Soucaille,[‖] Isabelle Meynial-Salles,[‖] Hervé Bottin,[⊥] Luca de Gioia,[▽] Maurizio Bruschi,[‡] Vincent Fourmond,[†] Christophe Léger,[*,†] and Luca Bertini*[,▽]

† Aix Marseille Univ., CNRS, BIP UMR 7281, Marseille, France
‡ Department of Earth and Environmental Sciences, Milano-Bicocca University, Piazza della Scienza 1, 20126 Milan, Italy
‖ Université de Toulouse, INSA, UPS, INP, LISBP, INRA:UMR792,135 CNRS:UMR 5504, avenue de Rangueil, 31077 Toulouse, France
⊥Institut de Biologie Intégrative de la Cellule (I2BC), Institut Frédéric Joliot, CEA, CNRS, Univ Paris-Sud, Université Paris-Saclay, F-91198, Gif-Sur-Yvette cedex, France.
▽ Department of Biotechnologies and Biosciences, University of Milano-Bicocca, Piazza della Scienza 2, 20126 Milan, Italy

* christophe.leger@imm.cnrs.fr
* luca.bertini@unimib.it

Table of contents

1 - DFT and TDDFT

1.1 - Fe_2S_2 models and DFT level of theory

Models. In this paper we used two different Fe_2S_2 models. To identify the main photochemical pathways along the excited surfaces we investigated the **H_{ox}** $[Fe_2(\mu\text{-adt})(SCH_3)(CO)_3(CN)_2]^{2-}$ model complex (adt = azadithiolate), while we investigated the relative stability of the possible photoproducts with a large model in which the same Fe_2S_2 model cluster was embedded in a 45-residues shell.

Small Fe_2S_2 model. This model was obtained from the full Fe_6S_6 H-cluster model in which the Fe_4S_4 cubane has been deleted, leaving a coordinated methylthiolate group coordinated to the proximal Fe atom. We consider the SCH_3^- instead of the $HSCH_3$ in order to avoid the unrealistic dissociation of this ligand during the geometry optimization along the distal or proximal CO dissociation coordinates.

In the figure below we report the main bond distances computed at the PBE0/TZVP level, which is the best hybrid DFT level, on the basis of the benchmark reported in the following section.

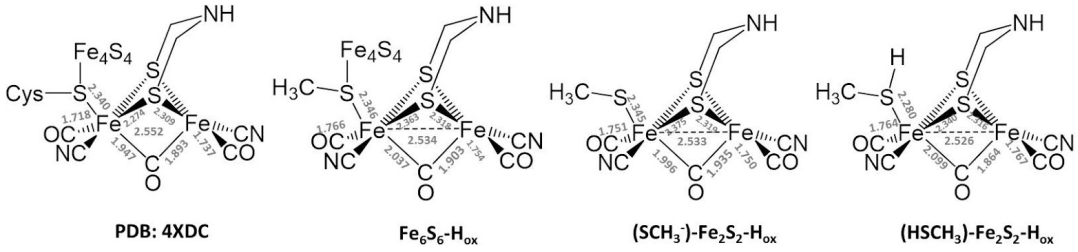

Figure S1 *- Comparison between the crystallographic structure of the diiron site (PDB: 4XDC) and the structures of the PBE0 optimized models.*

We compared the 4XDC PDB crystallographic structure with the Fe_6S_6-H_{ox} model and the SCH_3^- and $HSCH_3$ Fe_2S_2-H_{ox} models as described above. All the three optimized model structures are in good agreement with the crystallographic structures. More importantly for the computations presented in this paper, replacing SCH_3^- with $HSCH_3$ has no effect on the other structural parameters and, in particular, the SCH_3^- better reproduces the Fe-S bond length in the Fe_6S_6 model.

Large Fe_2S_2 model. The large model consists of 487 atoms and was obtained by embedding the small model in a 45-residues shell built from the structure of the FeFe hydrogenase from *D. desulfuricans* (pdb 1HFE[1]).

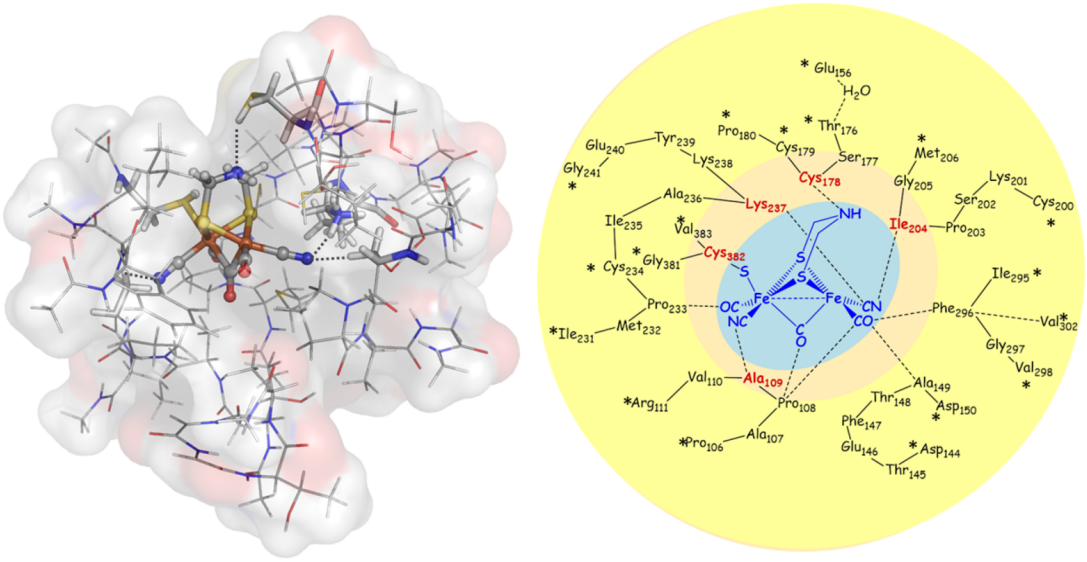

Figure S2 *- The large model for DFT computations on the unsaturated H_{ox} and H_{red} forms. (On the left) Structure of the large model, the Fe_2S_2 small model is shown as spheres and sticks, the five residues of the inner shell that form H-bonds with the active site as sticks (Ile 204, Ala 109, Cys 382, Cys 178 and Lys 237, D. desulfuricans numbering), the other residues included in the model are shown as lines. (On the right) In blue the Fe_2S_2 core; in red the first-shell residues directly interacting with the Fe_2S_2 cluster through H-bonds or Fe-S bond (Cys 382); in the light yellow band the second 44 residues shell. This second shell is made of 9 clusters (Asp144-Asp150, Pro106-Arg111, Ile231-Gly241, Gly381-Val383, Glu156, Trp156-Pro180, Cys200-Met206, Ile295-Val298, Val302,). The Cα of the terminal residues of each cluster (indicated with an asterisk) have been constrained to their X-ray positions. Glu156 and Trp156 interact with a water molecule which is present in the pdb file.*

The shell is divided into two parts. The inner shell includes the five residues (Ile204, Ala109, Cys382, Cys178 and Lys237) that form an H-bond network with the CN^- and the ADT of the Fe_2S_2 subcluster. In turn, the Fe_2S_2 subcluster and its first shell residues are encapsulated in a 40 residues sphere which maintains the first shell residues in their crystallographic position, avoiding unrealistic conformational rigidity imposed by constraints during the geometry optimizations. This last point allow us to predict the structure of the CO dissociation photoproduct. Indeed we need to leave the first-shell residues free to rearrange after CO dissociation to estimate the relative stability of the unsaturated Fe_2S_2 subcluster structures. The second shell also contains a water molecule H-bonded to Cys169 and Glu141, which is conserved in the crystallographic structures, and is part of the proton transfer chain[2,3].

The optimized geometry of the Fe_2S_2 core in the model of H_{ox} reproduces well the crystallographic data as the RMSD calculated with respect to the X-ray structure of the binuclear cluster in the semisynthetic enzyme from CpI (PDB code 4XDC)[4], assigned to the H_{ox} redox state, is equal to 0.19 Å Regarding the outer shell residues, the RMSD calculated including all of the (non-hydrogen) atoms is equal to 0.86 Å and 0.95 Å for the H_{red} and H_{ox} models, respectively, which is acceptable considering the very small number of atoms

constrained to the crystallographic positions in the geometry optimizations. The most relevant conformational change observed in the geometry optimized models of both H_{ox} and H_{red} is a significant displacement of the side chain of Phe 296 (equivalent to *Cr* F290) compared to the crystallographic position: in the optimized geometries the side chain of this residue moves about 3 Å away from the Fe_2S_2 core. The displacement of Phe 296 increases the size of a pocket close to Fe_d, which may accommodate the CO ligand after the photo-dissociation. It is worth noting that Phe 296 is embedded in our large model, and outer residues, such as Val 302 and Cys 200, should prevent any unrealistic movement of its side chain. In the H_{ox} and H_{red} models we also observed a rotation of the Cys 179 side chain that increases the distance between the Fe_2S_2 and the thiol group by more than 1.0 Å with respect to the X-ray value, probably due to a different pattern in the H-bond network.

Level of theory. We carried out the computations using two different levels of theory depending on the model system to be investigated. The DFT and TDDFT computations were carried out on the small model to explore its excited state PES along selected bond elongation coordinates. In this case, we performed the computation using the hybrid Generalized Gradient Approximation (GGA) PBE0[5] DFT functional as implemented in the TURBOMOLE suite of programs[6]. Basis sets of triple-ζ plus polarization split valence quality[7] were adopted for all atoms in the model.

Excited PESs have been scanned along selected Fe-Ligand (Fe-L) bond stretching coordinates as follows. For each step, the ground state structure was first optimized by keeping the elongated Fe-L distance fixed. The sampling of the excited PES has been carried out with a step of 0.05 Å, until complete ligand dissociation. For each point the vertical excitation energies have been computed and the resulting profile for each excited state is the approximation of the stretching coordinate on the excited surface using the structures computed on the ground state surface.

DFT calculations on the large model have been carried out using the BP86[8,9] functional combined with the Resolution of Identity (RI) technique in order to save CPU time.[10]

The DFT functional for the TDDFT computations was chosen on the basis of the comparison between the X-ray structure of the Fe_2S_2 subcluster and the binuclear H_{ox} model optimised at DFT level, using a set of functionals usually adopted in the computational investigation of FeFe hydrogenase models.[11–13]

We compare the *in vacuo* geometries and energies optimized with these DFT functionals, namely the pure GGA BP86[8,9], pure Perdew–Burke–Ernzerhof PBE functional and the corresponding 25% Hartree-Fock exchange (E_X^{HF}) hybrid PBE0[5], the hybrid B3LYP[9,14] functional, the meta-hybrid GGA M06 and M06-2X[15] functionals with 27% and 54% E_X^H respectively, and TPSS and the corresponding hybrid TPSSh[16,17] with 10% E_X^H. All computation were carried out using the def-TZVP basis set[18].

In this comparison our goal is to identify the best hybrid functional for the exploration of the excited state properties of the system. Indeed, it is known that pure functionals better reproduce experimental geometries of the H-cluster and of the corresponding models. In particular in this work it was crucial to find the hybrid functional that stabilizes the full-rotated form (see figure S3, left), which is the inverted square pyramids edge-shared Fe coordination in the Fe_2S_2 core of the H-cluster, with respect to the semi-rotated form. These

two coordinations can be described by the S-Fe-Fe-CN dihedral angle which measures the rotation of the SCH_3^- ligand respect to the cyanide around the Fe-Fe bond axes.

The comparison among the various optimized forms has been made on the basis of the absolute values of the differences between the H_{ox} X-ray structure (PDB code: 4XDC[4]) and computed Fe-Fe, Fe-S and Fe-C bond distances for the Fe_2S_2 model. All the results are reported in Table 1. First, we observe that all the hybrid functionals predict the stabilization of the full-rotated form with the exception of M06-2X, for which the calculated geometry is in very poor agreement with the crystallographic data. Starting from the full-rotated form, using pure functionals, the optimization converges to the semi rotated form except for TPSS. Among the complete set of functionals, TPSS gives the best agreement with X-ray data, while among hybrid functionals PBE0 is the best choice, while B3LYP and the two meta GGA M06 and M06-2X give the worst results. For these reason, TDDFT calculations were carried out using the PBE0 functional.

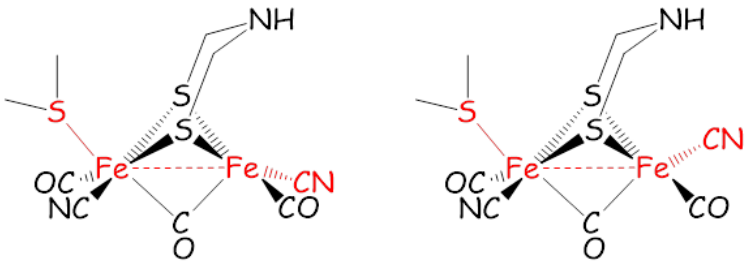

Figure S3 *- The full rotated and the semi-rotated forms described by the S-Fe-Fe-CN dihedral angle (around 100 degree for the full rotated and 40 degree for the semi-rotated).*

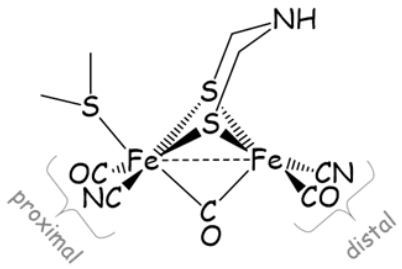

1.2 - Fe_2S_2 Small model MO populations

In the following panel, we report for each alpha and beta FMOs involved in the electronic spectrum (95α-111α; 94β-108β) the atomic/ligand (2Fe, distal and proximal CO, distal and proximal CN^-, the 2S that belong to the ADT ligand, the $SCH3^-$) mulliken orbital populations. From these values we can observe:

1) on average occupied FMOs 2Fe populations are always higher than those of the virtual FMOs.

2) on average occupied FMOs distal and proximal CO populations are always lower than those of the virtual FMOs.
3) on average the 2S and SCH_3- contributions are slightly lower for virtual FMOs
4) for all the FMOs considered, the CN^- contributions are low.

The 102α and 101β orbitals aree mainly composed by the lone-pairs strongly localized on the S atom that belong to the $SCH3^-$ ligand. This fact could be considered as an artifact since in the H-cluster the bonding network of the atom is saturated by the Fe4S4 cluster.

On the basis of these MO population, we can conclude that the excitations that involve these FMOs will be characterized by

1) charge transfer (CT) from Fe to both CO ligands;
2) CT from sulfur ligands to CO ligands

Table S1 *- In vacuo geometries energies optimized with the following DFT functionals: PBE0, BP86, B3LYP, TPSSh, TPSS, M06 and M06-2X.*

		XRD	PBE0	δ	PBE	δ	BP86	δ	B3LYP	δ	TPSSh	δ	TPSS	δ	M06	δ	M06-2X	δ
Fe-Fe		2.552	2.533	0.019	2.520	0.032	2.530	0.022	2.599	0.047	2.541	0.011	2.551	0.002	2.550	0.002	2.881	0.329
Fe-S	**prox front**	2.321	2.374	0.053	2.379	0.058	2.345	0.024	2.424	0.103	2.378	0.057	2.385	0.064	2.380	0.060	2.511	0.190
	prox back	2.274	2.357	0.084	2.338	0.065	2.390	0.117	2.408	0.134	2.355	0.082	2.354	0.081	2.382	0.067	2.500	0.226
	dist front	2.289	2.319	0.030	2.323	0.034	2.314	0.024	2.361	0.072	2.317	0.028	2.315	0.026	2.340	0.065	2.473	0.184
	dist back	2.309	2.333	0.024	2.308	0.001	2.330	0.021	2.373	0.064	2.334	0.025	2.335	0.025	2.355	0.060	2.362	0.053
Fe-SCH_3		2.340	2.345	0.005	2.362	0.022	2.370	0.030	2.397	0.057	2.356	0.016	2.363	0.023	2.369	0.029	2.497	0.157
Fe-C	**dist**	1.737	1.750	0.013	1.744	0.007	1.746	0.009	1.769	0.032	1.755	0.018	1.751	0.014	1.770	0.033	1.889	0.152
Fe-C	**prox**	1.718	1.751	0.033	1.742	0.024	1.744	0.026	1.768	0.050	1.755	0.037	1.753	0.035	1.772	0.054	1.930	0.212
μ-CO		1.947	1.996	0.049	1.976	0.029	1.979	0.032	2.043	0.096	1.999	0.052	1.989	0.042	2.040	0.092	2.117	0.170
		1.893	1.935	0.042	1.923	0.030	1.926	0.033	1.954	0.061	1.936	0.043	1.931	0.038	1.942	0.049	2.171	0.278
Fe-CN	**dist**	1.911	1.923	0.012	1.916	0.005	1.912	0.001	1.949	0.038	1.928	0.017	1.922	0.011	1.950	0.039	2.070	0.159
Fe-CN	**prox**	1.841	1.936	0.095	1.909	0.068	1.918	0.077	1.965	0.124	1.939	0.098	1.935	0.094	1.940	0.099	2.100	0.259
Sum				0.457		0.375		0.415		0.877		0.483		0.455		0.650		2.368
S-Fe-Fe-CN			110.2		40.02		41.2		107.6		108.5		106.6		108.6		35.5	

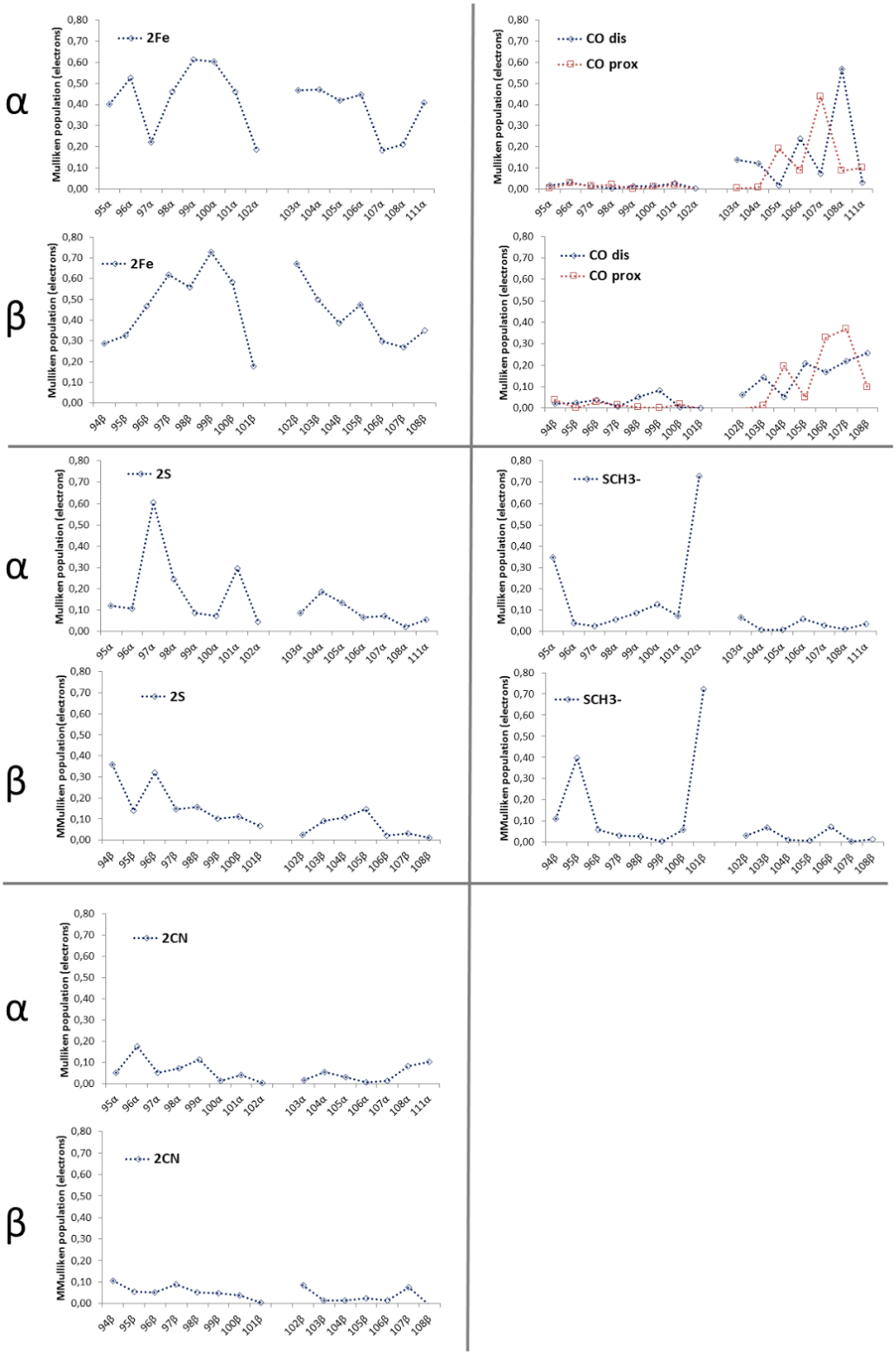

Figure S4 - *Atomic/ligand (2Fe, distal and proximal CO, distal and proximal CN^-, the 2S that belong to the ADT ligand, the $SCH3^-$) mulliken orbital populations of alpha and beta FMOs involved in the electronic spectrum (95α-111α; 94β-108β).*

In figure S5 we report the isosurfaces of the 3 highest occupied and the 3 lowest unoccupied MOs. The virtual MOS are characterized by antibonding-non bonding combinations between Fe and S of ADT atomic orbitals and non-bonding/antibonding combinations between Fe and distal or proximal CO orbitals.

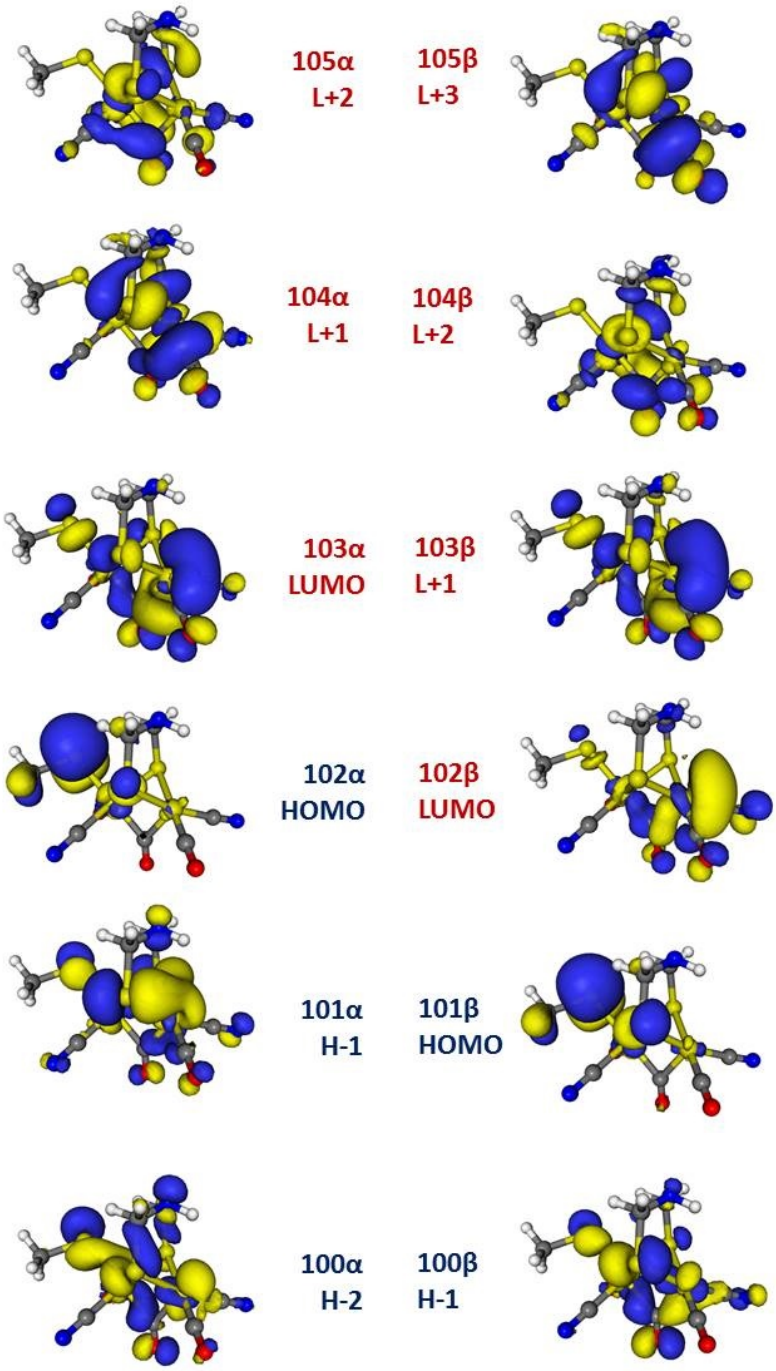

Figure S5 - *Isosurfaces of the first 6 FMOs around the HOMO/LUMO gap.*

1.3 - Fe_2S_2 Small model electronic spectra.

Table S2 *- SCH_3^- Fe_2S_2 model TDDFT electronic spectrum. For each transition we list the excitation energy λ (**nm**), the oscillator strength (**f**) and the main monoelectronic excitations (**1e**) with the corresponding percentage composition, band assignment and localization of the Charge Transfer (CT)*

n. ex	λ (nm)	f	1e	Assignment
1	1413	$1\cdot10^{-2}$	100β → 102β (50.1%) 99β → 102β (21.1%)	LLMCT
2	988	$1\cdot10^{-3}$	99β → 102β (21.6%) 99β → 103β (12.2%)	LLCT
3	890	$1\cdot10^{-4}$	98β → 102β (45.8%) 97β → 102β (16.7%)	LLMCT
13	547	$1\cdot10^{-2}$	102α → 103α (18.7%) 101α → 103α (14.0%)	LLMCT
19	432	$2\cdot10^{-3}$	97β → 104β (11.0%)	MLCT
21	422	$1\cdot10^{-2}$	100β → 105β (11.0%)	MLLCT
24	404	$1\cdot10^{-2}$	100α → 103α (13.0%)	MLLCT
25	392	$1\cdot10^{-2}$	98α → 103α (10.4%)	LLMCT
27	383	$2\cdot10^{-2}$	100β → 103β (13.4%)	MLCT
28	378	$1\cdot10^{-2}$	100α → 103α (6.8%) 99α → 103α (6.7%)	MLLCT
29	366	$1\cdot10^{-2}$	95β → 102β (31.5%) 101β → 103β (10.4%)	LMCT
66	279	$2\cdot10^{-2}$	101α → 106α (4.4%)	LLCT
70	274	$3\cdot10^{-3}$	100α → 106α (5.7%)	MLCT
88	256	$2\cdot10^{-2}$	101β → 111β (6.3%) 98α → 107α (5.0%)	LLMCT MLLCT
95	251	$1\cdot10^{-2}$	97α → 104α (5.7%)	LMCT

Table S3 *- MO differential populations computed according to the TDDFT main one-electron excitations of the Fe_2S_2 small model for selected excited states.*

	1ex	**2ex**	**3ex**	**13ex**	**19ex**	**21ex**	**24ex**	**25ex**	**27ex**	**28ex**	**29ex**	**66ex**
2·Fe	0,05	0,00	0,07	0,10	-0,07	-0,03	-0,03	0,04	0,02	0,03	0,16	0.00
2·S	-0,06	-0,03	-0,09	-0,05	0,00	0,00	-0,03	-0,01	0,00	0,00	-0,06	-0.05
SCH_3^-	-0,03	-0,05	0,00	-0,18	-0,02	-0,04	-0,02	-0,16	-0,15	-0,11	-0,22	-0.06
CO dist	0,03	0,02	0,02	0,05	0,02	0,06	0,07	0,04	0,05	0,05	0,06	0.04
CO prox	-0,01	0,00	-0,01	0,00	0,07	0,01	0,00	0,04	0,03	0,01	0,00	0.05
μCO	-0,01	0,05	0,05	0,08	0,04	0,01	0,07	0,06	0,05	0,05	0,07	0.03
$2CN^-$	0,03	0,01	0,02	0,01	-0,03	-0,01	-0,02	0,00	-0,01	-0,01	0,00	0.00
$CH_2NH\text{-}CH_2$	0,00	0,00	-0,06	-0,01	-0,01	-0,01	-0,03	-0,01	-0,01	-0,01	-0,01	-0.05

Figure S6 shows i) the computed electronic spectra of the SCH_3^- and $HSCH_3$ Fe_2S_2 small models at PBE0 level ii) the computed electronic spectra of the SCH_3^- computed at PBE0 and TPSSh levels. The aim of the first comparison is to underline the small effect of the ligand choice in modelling the Fe-S-Cys bond network to the Fe_4S_4 cluster, while the second comparison is useful to figure out the variability of the computed excitation energies as a function of the DFT functional adopted. In particular in the latter we consider the comparison between two hybrid functionals (PBE0 and TPSSh) which has been shown to better reproduce the H-cluster geometry in the H_{ox} state.

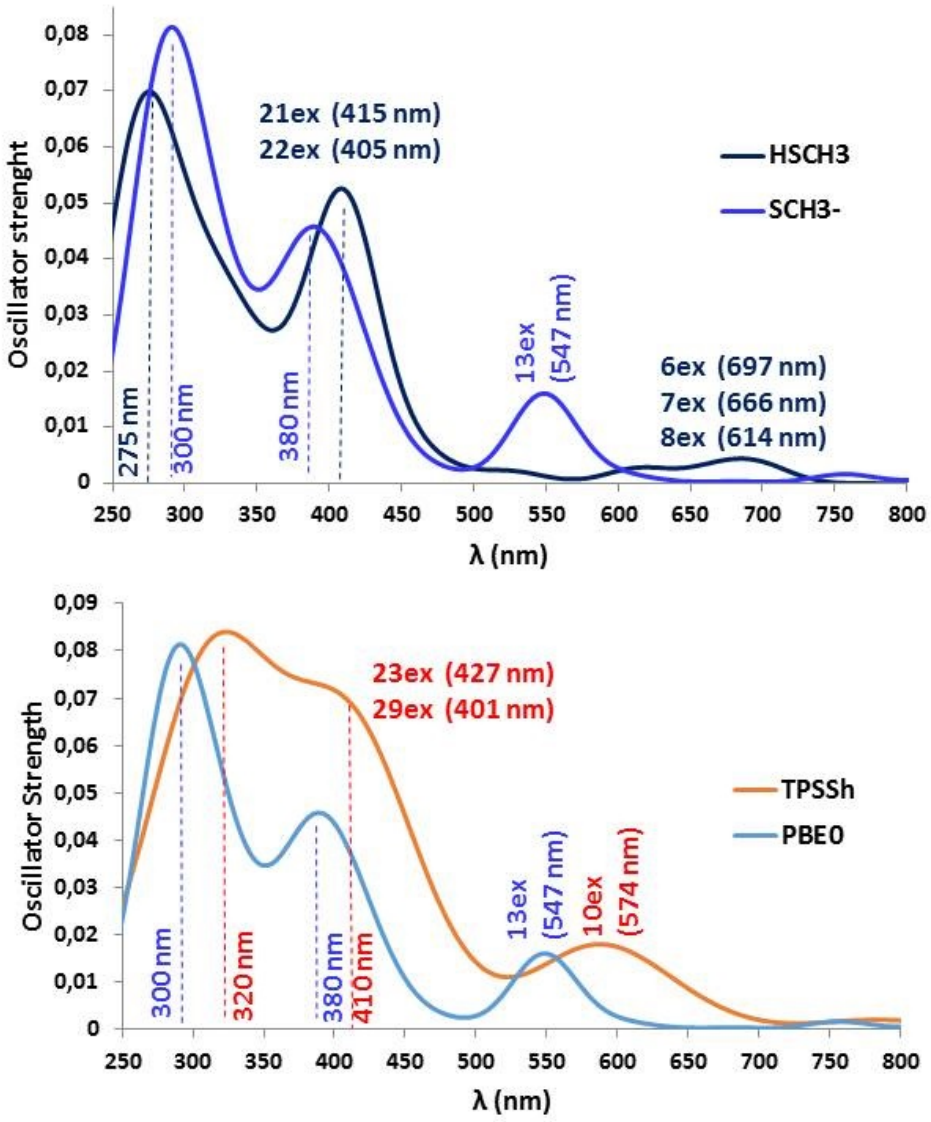

Figure S6 *- Hox Computed Spectra Superimpositions. On top the comparison between the computed spectra (PBE0) of the $HSCH_3$ and SCH_3^- Fe_2S_2 models to evaluate the effect of the two ligands; on bottom the comparison between SCH_3^- Fe_2S_2 model PBE0 and TPSSh spectra computed with the corresponding minimum geometries.*

From the comparison with the $SCH3^-$ spectrum emerges that the $HSCH_3^-$ spectrum presents:

1) a bathochromic shift of the first intense feature of around 23 nm;
2) an hypsochromic shift of the second intense feature of around 17 nm;

The weak feature computed for the $HSCH_3$ model is characterized by a three excitations of similar intensity and therefore this band results broad compared to the SCH_3^- model. We estimate a bathochromic shift in a range between 100 to 150 nm. Regarding the nature of the MO involved in the spectrum, it is useful to compare MO population for SCH_3^- and $HSCH_3$ models (figure S7).

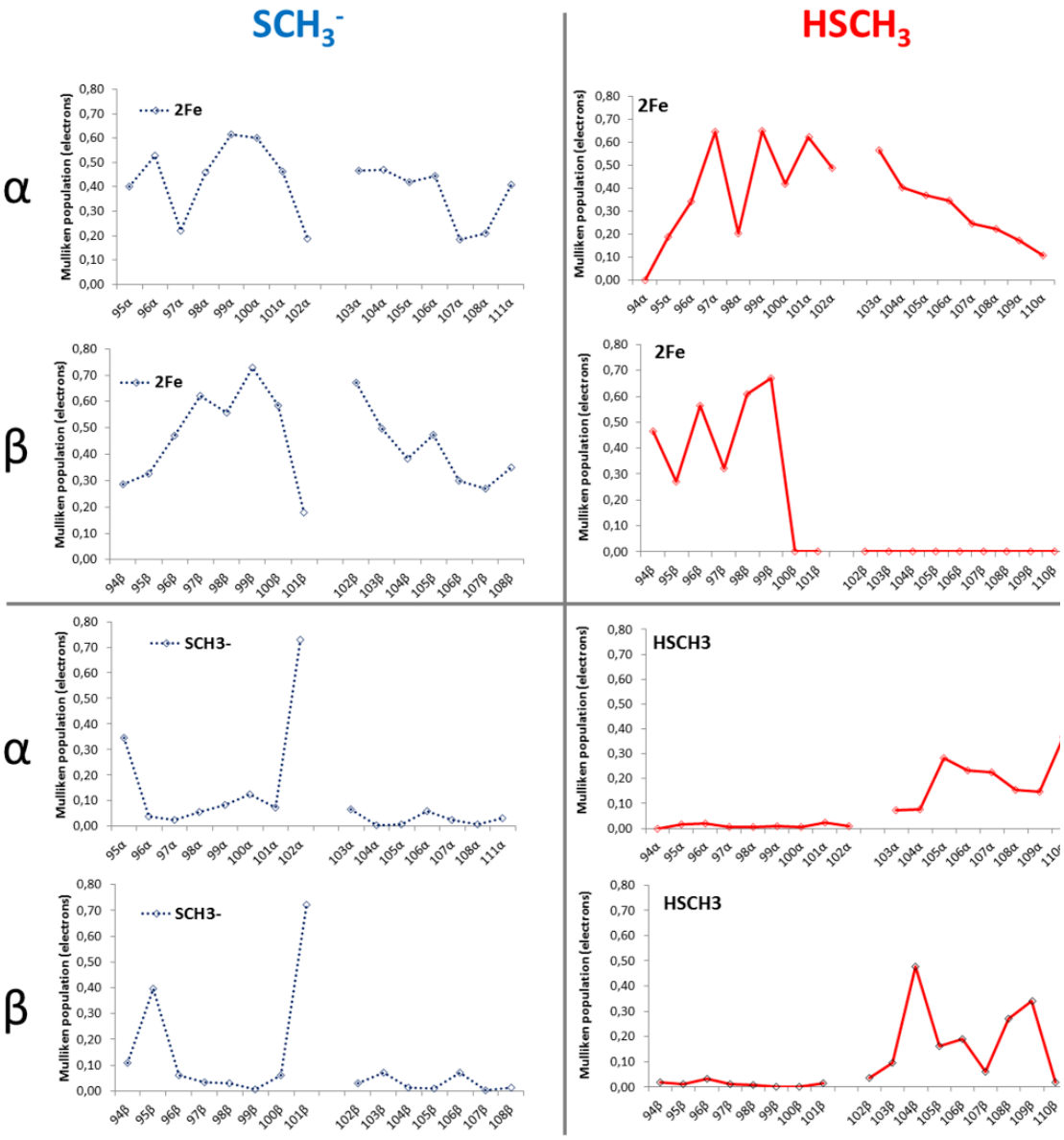

Figure S7 *- MO populations for the iron atoms and the $HSCH_3$/SCH_3^- ligand.*

It is important to note that the FMOs involved in the electronic spectrum of the two models are similar except for the $SCH3^-$ population of the HOMO in the SCH_3^- Fe_2S_2 model, due to the negative charge on this ligand. This is probably the reason why the weak feature changes significantly between the two models.

Table S4 *- Differential populations for the excitation involved in the weak feature of the PBE0 computed electronic spectra for the $HSCH_3$ and SCH_3^- Fe_2S_2 model (13ex state for SCH_3^- model; 6ex-8ex for $HSCH_3$ model).*

	$HSCH_3$			SCH_3^-
	6ex	**7ex**	**8ex**	**13ex**
2Fe	0.05	-0.01	0.02	0.1
2S	-0.09	-0.03	-0.09	-0.05
HSCH3/ SCH_3^-	0.02	0.04	0.03	-0.18
CO dist	0.03	0.06	0.03	0.05
CO prox	-0.01	0.00	0.00	0
μCO	0.03	0.00	0.06	0.08
adt	-0.02	-0.04	-0.01	-0.01
2CN-	-0.02	-0.02	-0.02	0.01

The comparison among differential populations (Table S4) of the 13ex state for the SCH_3^- model ands the 6ex-8ex for the $HSCH_3$ Fe_2S_2 model indicates that the nature of these excitations is similar and can be assigned in both case to a LLMCT band which involves the sulfur ligands.

We also computed the spectrum of the SCH_3^- Fe_2S_2 model with theTPSSh hybrid functional, starting from the minimum geometry obtained with the same functional (Figure S6). The TPSSh spectrum shows a broadening and an average ~20-30 nm bathochromic shift of the peaks compared to the PBE0 one.

Regarding the comparison of the spectra computed with different models and different functionals presented above we observed that

- the effect of the $HSCH_3$ ligand compared to SCH_3^- ligand
    - is more significant for low energy states which involve CT from the sulfur atoms, mainly due to the negative charge localized on the SCH_3^- ligand in the HOMO;
    - is less significant for higher energy states which involve the CO ligands;
- considering two hybrid functional which better reproduce the X-ray H-cluster geometry in the Hox state, the effect is a general red shift of 20-30 nm, while the nature of the excitations are similar

1.3 - Small model TDDFT geometry optimizations of 1ex and 2ex

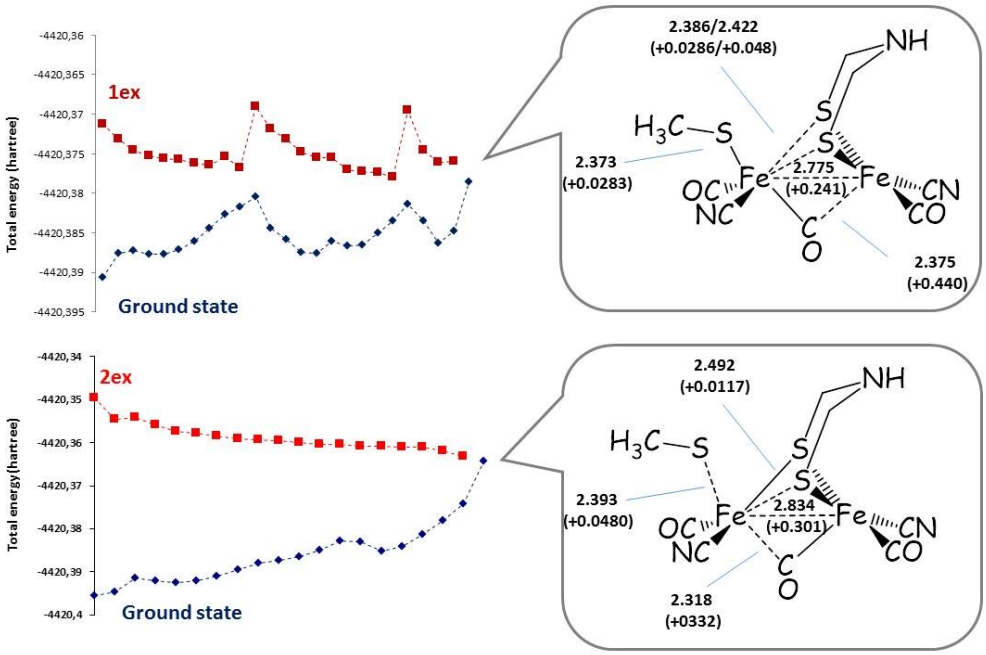

Figure S8 *- 1ex and 2ex TDDFT geometry optimizations of the* SCH_3^- Fe_2S_2 *model and internal conversion between the excited states and the ground state. On the left are shown the geometriesat the intersection point (distances in Å).*

1.4 - CO dissociation energy barriers

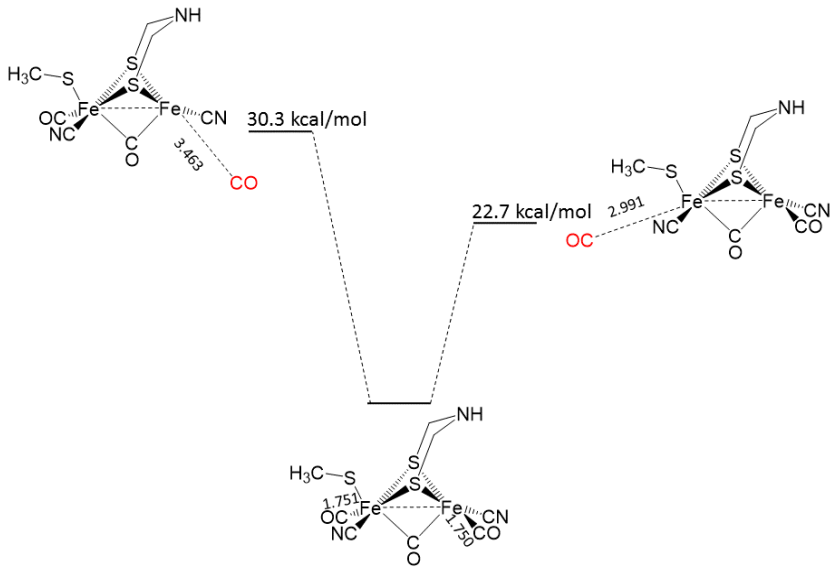

Figure S9 *- Small model [-]SHC3-Fe_2S_2-Hox structures of transition states and free energy barriers (in kcal/mol) for the dissociation of CO in proximal or distal position. The imaginary frequencies of the normal modes that describes the dissociation are 188.10 cm^{-1} for CO_{distal} and 171.59 cm^{-1} for CO_{prox}. Distances in Å.*

1.5 - Large Fe_2S_2 model structures

Compared to the crystallographic structure, the large model in the H_{ox} state shows a decrease of the d(Fe-Fe) of 0.03 Å and of the d(Fe-SCH3$^-$) of 0.20 Å (0.17 Å in H_{red}). The distance between both the Fe atoms and the bridging CO is lower in the model in H_{ox} state than in the one in H_{red} state. In the latter structure the distances between the Fe atoms and the two terminal CO is lower (-0.03 Å). The relative stability of the H_{ox}^{uns} and H_{red}^{uns} forms correlates with the Fe-Fe bond distances.

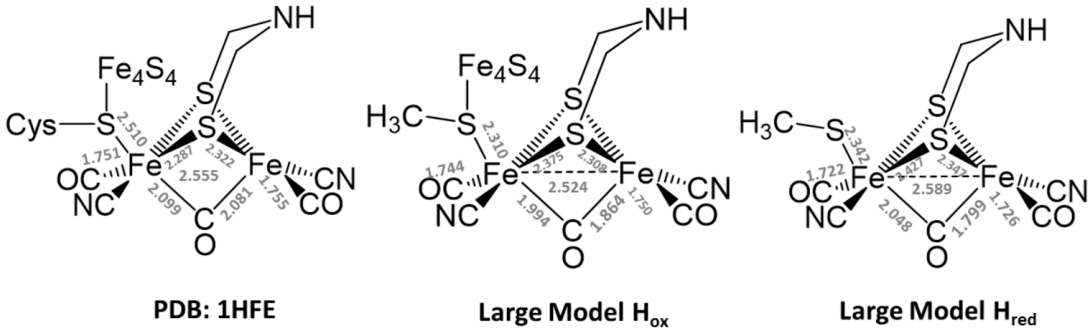

Figure S10 - *Comparison between the crystallographic structure of the diiron (PDB: 1HFE) and the structures of H_{ox} and H_{red} large models optimized with BP86. The bridging CO was added manually.*

Table S5 *- Resume of the optimizations of H_{red}, H_{red}^{uns},H_{ox} and H_{ox}^{uns} with the large model.*

	ΔE (kcal/mol)	**Fe-Fe (Å)**	**E(HOMO) eV**	**E(LUMO) eV**
H_{red}	-	2.589	-0.8763	-0.2948
H_{red}^{uns}				
1	1.5	2.491	-0.7522	-0.0109
2	5.4	2.542	-0.5661	-0.0314
3	0.0	2.487	-0.6246	-0.0773
4	5.5	2.616	-0.8431	-0.0403
H_{ox}		2.524	-3.2200	-2.3390
H_{ox}^{uns}				
1	1.1	2.477	-2.9939	-2.4305
2	5.2	2.512	-3.0259	-2.3739
3	0.0	2.473	-3.0256	-2.5882
4	7.3	2.516	-3.2436	-2.3835

1.6 - H_{red}^{uns} protonated

We added a proton in apical position on the Fe_d or in bridging position (μH^+) between the two Fe atoms of H_{red}^{uns} form 3 (see main text fig. 6).
The optimized structures show that the binding of a proton in bridging position increases the d(Fe-Fe) by 0.03 Å and decreases the d(Fe-SCH_3^-) by 0.11 Å.

Table S6 *- Relative energies and geometries of the optimized H_{red}^{uns} large model protonated in bridging or apical position.*

	ΔE (kcal/mol)	**Geometry**
H_{red}^{uns}+ μH+	0.0	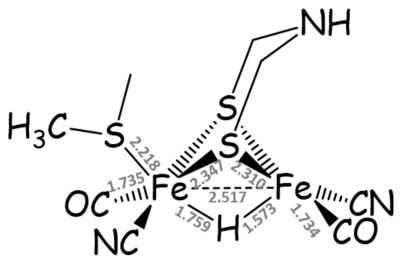
H_{red}^{uns}+ terminal H^+	8.7	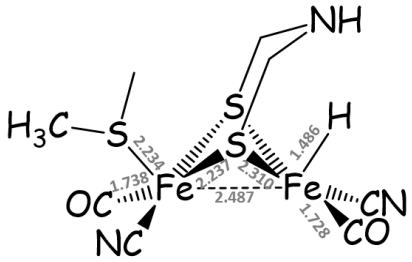

1.7 - Optimized coordinates PBE0

Model	**Coordinates (atomic units)**			
Fe_6S_6 Hox	5.81080535014191	57.71989686707392	57.15329373990119	fe
	4.56923642638079	53.76857326697451	55.50449599980489	s
	4.09574087336189	49.75056306718419	61.69169390413702	s
	1.22675081023325	51.52425806414441	62.47653240855141	c
	0.05957048648522	50.37891642183153	63.73914444090592	h
	0.13852876167692	51.95269733797753	60.77839064051678	h
	1.69932025054731	53.29465150501215	63.42077582536746	h
	6.23254409710555	52.78497754335533	59.43363392216826	fe
	6.62274958572854	56.61301155777577	61.38350567012471	s
	3.31475779156671	61.24350983742652	56.66140784174710	s
	5.11690799766659	63.79853370306723	58.10231438207044	c
	3.80394091849611	65.25631296786922	58.73334779018125	h
	6.39862310644849	64.62644814666206	56.72223982409638	h
	6.17171580452207	63.02495732454117	59.69593080371398	h
	0.50900771683444	63.01602809310312	53.72229190704493	fe
	-4.19978684473726	63.86309387550450	53.50640002830279	fe
	-1.74424845309392	64.43447673102126	50.94267387678887	c
	-1.56314667773619	65.09584346105135	48.85622281948916	o
	2.54348025941173	66.00749115871449	53.28358857478921	c
	3.75800215885071	67.81581405096499	52.99201975772895	n
	2.16084281768218	61.48146058456630	51.26090361105130	c
	3.27436358700570	60.53651327544893	49.66997100055659	o
	-6.93734638116288	62.66136591715383	51.40328172477759	c
	-8.71725141685268	62.01983403549868	50.28243425987739	n
	-5.37826336014119	66.95043634531818	53.25988839316993	c
	-6.18568874059059	68.96406121524875	53.08864763528491	o
	-2.54893750388723	59.81880851117124	54.05213815477550	s
	-2.87173221635250	58.89329734324012	57.41025018069697	c
	-3.91408058605852	60.73030342603185	59.11489951384597	n
	-2.31492395388705	62.86830548483168	59.56652027827633	c
	-1.77534213333574	65.11652003883135	56.93191448610050	s
	-1.00259604415644	58.34274267937512	58.08582698216033	h
	-4.08679757798368	57.22654011765098	57.39087163789797	h
	-5.61116560583823	61.32595816032543	58.44668097298277	h
	-3.12359421566040	64.01195742344419	61.08420686673453	h
	-0.45838059062679	62.18186717297962	60.15389069210528	h
	10.61171214850794	55.95599956902353	59.52802788194847	fe
	10.23645542182041	51.65031868271000	58.27742266937483	s
	10.61549203367422	53.39594103716555	51.22157558567349	s
	11.13802353453915	56.44722608869662	49.69618905785286	c
	11.86496663632045	56.10359660186386	47.79255932189610	h
	12.50015012448194	57.57102434119471	50.75696994210393	h
	9.37943809340065	57.51103973978702	49.56061114019386	h
	8.77639275916412	53.93351825835913	54.96839088038901	fe
	9.86458440762793	57.95530088241556	55.77206113890549	s
	14.36203058884170	56.96374224126133	61.29573280848008	s
	14.28459661333639	60.41959110895603	61.46950426013920	c
	14.12494266828041	61.23470731006492	59.58090331227831	h
	12.68101786787739	61.07102017683486	62.59302710565727	h
	16.02618934521948	61.11195593527371	62.34435841142183	h

Fe_2S_2 HSCH3 Hox	-41.89483001187321	24.27246369648162	-6.59968171955257	h
	-42.23124559492533	24.12206420046604	-8.62519453892029	c
	-45.19763204959049	25.67650830423168	-9.41526752559436	s
	-46.01790372829429	25.31497882403544	-13.63038674788717	fe
	-49.07107035899867	27.19518728782347	-16.78034428790611	fe
	-48.10615547945212	29.13299525046998	-19.32279542501628	c
	-47.49168472055619	30.37686844152859	-20.97930148182353	o
	-46.72030261477788	29.66230859773901	-14.03457069682950	s
	-48.86928362146091	30.74814975443858	-11.48502813550091	c
	-51.40481877533840	29.81030092866806	-11.44312273429892	n
	-51.65171637492350	27.17313077631185	-10.91241488105048	c
	-50.39001432074159	24.88642366741519	-13.25745316070968	s
	-45.54309019925829	22.01594175719755	-13.61858455593900	c
	-45.17723440838752	19.88590856071344	-13.53971873714446	o
	-42.49457988000159	25.88348061428108	-14.30479958876543	c
	-40.32706303490400	26.17531990591256	-14.50048180054212	n
	-46.58195752655830	24.81678372177757	-17.52436196945557	c
	-45.70423423138875	23.54298352496140	-19.07329574677895	o
	-51.76114250099297	25.85350802902154	-18.81668907910437	c
	-53.47441820345225	25.19888298967419	-20.02272426123754	n
	-40.78063215095271	25.11566283516829	-9.69454241549364	h
	-42.25778703486431	22.15622269906594	-9.23052352249227	h
	-48.91378742133644	32.80033297750255	-11.67820169630326	h
	-47.96792822338090	30.29893319738160	-9.68020316408842	h
	-50.76991251663671	26.78817444933226	-9.08199922334755	h
	-53.65386471847027	26.70462783618898	-10.76082053530716	h
	-52.30442665222658	30.23933927948188	-13.08052881839019	h
	-46.73218660859112	23.95965048506881	-8.30194319770306	h
Fe_2S_2 $SCH3^-$ Hox	-42.14014888682988	24.81903368870568	-6.55843948338223	h
	-42.34115600628162	24.79551816714691	-8.61787864323274	c
	-45.69833764354120	24.98211600379869	-9.36519186882416	s
	-46.17063215416918	25.12131808054645	-13.76874475696289	fe
	-49.11106309127288	27.28433914788062	-16.86613091548642	fe
	-47.97994571056324	29.19462524968080	-19.31686496339990	c
	-47.26366762897812	30.45915079058738	-20.94085459287275	o
	-46.67658975100058	29.57208772962775	-14.02947174318164	s
	-48.61831820921913	30.54232075440514	-11.29768969313551	c
	-51.22689573794887	29.77838298459196	-11.24999725392745	n
	-51.58718632585597	27.11249886994311	-10.86927969593362	c
	-50.60990880725217	24.95141216181075	-13.43855806063867	s
	-45.81916348560075	21.83998957665667	-13.52634496968008	c
	-45.52601512294183	19.69815621915812	-13.32422924581436	o
	-42.61763456609077	25.52824246486512	-14.41090506223367	c
	-40.45901968096822	25.72312239090870	-14.78537884986434	n
	-46.62841568797175	24.67263037615874	-17.48574267238756	c
	-45.90299316666369	23.41646003926634	-19.13746462299648	o
	-51.73701747218900	25.98352338599589	-19.05483948241723	c
	-53.39973752312307	25.38836995502340	-20.36637403655083	n
	-41.30339718075328	26.37631423496332	-9.43576821564560	h
	-41.50374571571272	23.05639683971169	-9.34875687844957	h
	-48.52210915675666	32.60583645080366	-11.24940297540919	h
	-47.67749265501912	29.76963575946598	-9.62616554138771	h
	-50.56590271803820	26.54819422135249	-9.16537857758022	h
	-53.60126464877966	26.74514975948060	-10.59522111809206	h
	-52.05864689692346	30.28691391139561	-12.90472290580486	h

Fe_2S_2 SCH3$^-$ Hox, CO_{dist} TS	-41.19300046591601	25.43257113408177	-6.97113356380049	h
	-41.65156518877431	25.08252015495216	-8.95836578569076	c
	-44.99919424619376	25.74610504541949	-9.43219004707211	s
	-45.91929056193898	25.34379180035880	-13.72351809963653	fe
	-49.32972655711102	26.87179789524427	-16.63130773044846	fe
	-46.85159639822878	30.61103867863389	-21.39630319712519	c
	-46.17022729512486	32.30263836484327	-22.50456710282637	o
	-46.83478161509836	29.75725852207002	-14.40196757586513	s
	-48.69262617839609	30.80571637511763	-11.64075644227662	c
	-51.19157167063207	29.77731985469673	-11.30590264070768	n
	-51.28219348733460	27.16078804356808	-10.57265299635153	c
	-50.26828927662681	24.73238413814658	-12.88784340915184	s
	-45.23423271342367	22.14841986719208	-13.33671383694843	c
	-44.70900223204944	20.06053705201204	-13.02319882287204	o
	-42.51932553926925	26.01814812978358	-14.81504281125261	c
	-40.44450451111973	26.39752198931716	-15.44268133122018	n
	-46.83491389592766	24.58445070728590	-17.53820241942934	c
	-45.99889338556066	23.32325126565028	-19.14120229589837	o
	-52.12269075891042	26.41842802952528	-19.14171063222812	c
	-53.79806903599511	26.29921654615832	-20.56274122045707	n
	-40.48140708304273	26.27592189211824	-10.16376350434840	h
	-41.20855669144192	23.11029235855700	-9.39204470510509	h
	-48.83182340534444	32.86311412832195	-11.77665042794469	h
	-47.55312698944445	30.31681398892199	-9.98631822047043	h
	-50.10620557648307	26.90524793752248	-8.89458374925361	h
	-53.23415964013297	26.68359440049179	-10.09220713460055	h
	-52.19824767888158	30.01561998923201	-12.92253311177322	h
Fe_2S_2 SCH3$^-$ Hox, CO_{prox} TS	-42.76502962079319	24.59151639329675	-6.26324971332606	h
	-42.85932128564578	25.22282476141439	-8.23105555057027	c
	-45.92967838649145	24.33296595352147	-9.53717567211071	s
	-46.17280299184399	25.34741440535554	-13.72037359535141	fe
	-49.05157398815932	27.14022593351615	-17.02444068595558	fe
	-47.91519284732694	29.16257115668157	-19.37153156560514	c
	-47.18486282984609	30.50294823355896	-20.93132852322415	o
	-47.14526172900534	29.70608662811761	-13.97128576209757	s
	-49.34870129721133	30.25219669353410	-11.30704214556581	c
	-51.83494216065592	29.16556259314993	-11.46223968368131	n
	-51.90374141997589	26.46599621574228	-11.17056990370108	c
	-50.56472683564031	24.53231505300571	-13.76218567576764	s
	-45.50298011541201	19.74147191228337	-13.49368204845045	c
	-45.07396504009365	17.94913470538211	-12.40678905558607	o
	-42.53010831658350	25.66965995416587	-14.06840445724496	c
	-40.33974187376482	25.79282852405509	-14.23989332435207	n
	-46.21102459260774	24.76137064729892	-17.37259249032164	c
	-45.27893985427549	23.52560880913808	-18.93105341156469	o
	-51.28831808973129	25.57419098993249	-19.45084904058075	c
	-52.73769268022738	24.80138181871050	-20.91500695861441	n
	-42.60832408122364	27.27080222984628	-8.29221464713498	h
	-41.32115980252218	24.37822111495182	-9.31034239574978	h
	-49.53367902945497	32.30488902866753	-11.14627369481057	h
	-48.42906040546413	29.51834611626769	-9.61073515155941	h
	-50.88120116084080	25.96338008700028	-9.44767257327884	h
	-53.87344076280525	25.86860276253154	-10.99404491644983	h
	-52.62410691155802	29.63788263252950	-13.14783382024038	h
Fe_2S_2 SCH3$^-$ Hox 1ex TDDFT opt	-42.23291577281307	24.64426102724795	-6.51737154425936	h
	-42.42276149801403	24.81775066668009	-8.57002922183962	c
	-45.77116056084986	24.98747578118977	-9.35544122745171	s
	-46.14462983178593	25.03858640842434	-13.82402415295839	fe
	-49.44781585728042	27.59541045502963	-16.98962426192003	fe
	-48.34099857738305	29.34013185984404	-19.54152264413848	c
	-47.64789809922925	30.51953618357089	-21.25876659082965	o
	-46.66491853655718	29.57251077991268	-14.16756730105891	s
	-48.48520862643780	30.48566690779161	-11.32116060271327	c

	-51.10162431511112	29.74059945440388	-11.17442662195609	n
	-51.49138817032071	27.06790040212913	-10.87580229601208	c
	-50.64713972391104	25.00526728499498	-13.58117345467749	s
	-45.80334835763745	21.76670959281920	-13.27221230449575	c
	-45.48438932050368	19.64490834132551	-12.97121886251824	o
	-42.55766384541911	25.41209741448089	-14.29282274461653	c
	-40.40346183628009	25.55524237427704	-14.70449580735343	n
	-46.17176091182996	24.53601021411533	-17.21199999513187	c
	-45.76165569991974	23.71574721242236	-19.16520386715170	o
	-51.93879812027477	26.13863567682524	-19.20877680814624	c
	-53.42043871441080	25.31153023388904	-20.62754862730374	n
	-41.42443599830314	26.50030964838855	-9.21424107168262	h
	-41.54176472914567	23.18049703677352	-9.46058380991491	h
	-48.37788963509716	32.54657744775455	-11.19226661133277	h
	-47.48418240187135	29.64593708437899	-9.72199962311221	h
	-50.44942608802315	26.42217497920943	-9.21640588981364	h
	-53.50185639984418	26.72676960520038	-10.55045072534256	h
	-52.02687400147013	30.33349514044842	-12.74866015735657	h
Fe_2S_2 SCH3$^-$ Hox 2ex TDDFT opt	-41.83531862905672	25.25497685670801	-6.39749214575473	h
	-42.29219599273127	24.75619464724957	-8.35696775328443	c
	-45.68383799919233	25.00798017438881	-8.91985180507533	s
	-46.01878658298919	25.06326476803541	-13.42910402951751	fe
	-49.23333678170825	27.44833201131398	-16.98812834151780	fe
	-47.94782000282129	29.24623927453920	-19.46388679778606	c
	-46.98336844663030	30.37520171879623	-21.08506081713042	o
	-46.66871566063519	29.66791267658789	-14.16899303251621	s
	-48.71911611119194	30.54837950507040	-11.45163437733478	c
	-51.28096991593460	29.65324874468129	-11.38125259185610	n
	-51.53287592770111	26.98228998337542	-10.95701024996854	c
	-50.49927283080810	24.84470877186597	-13.53164395062344	s
	-45.61832669824216	21.66548393326494	-13.57286549540757	c
	-45.18455673400410	19.55533970013837	-13.38948050866110	o
	-42.46231036749609	25.53533965821009	-14.26689192815017	c
	-40.37277365679314	25.82956374444990	-14.83461247734295	n
	-46.76344836569168	24.64230329110054	-17.72543727686801	c
	-46.11850214373743	23.31328726199412	-19.16198336214505	o
	-52.08368680075848	26.46053061112891	-18.98995116423571	c
	-53.91252359999846	25.96122712480640	-20.19237493513775	n
	-41.25738203931380	26.01215059914950	-9.63175119062951	h
	-41.63995918187405	22.81736924071702	-8.72259327262073	h
	-48.73120770120239	32.62104546846452	-11.42108980993395	h
	-47.73844584647877	29.82912991044687	-9.78063950927310	h
	-50.44760524968160	26.48203092598218	-9.27252505674842	h
	-53.53400493092188	26.55239104257138	-10.63250886033385	h
	-52.18605743951505	30.12581757263559	-13.01006608732005	h

2 - Absorption spectra of the filters

We recorded the absorption spectra of the two filters that we used with a PerkinElmer UV/vis lambda 25 spectrophotometer.

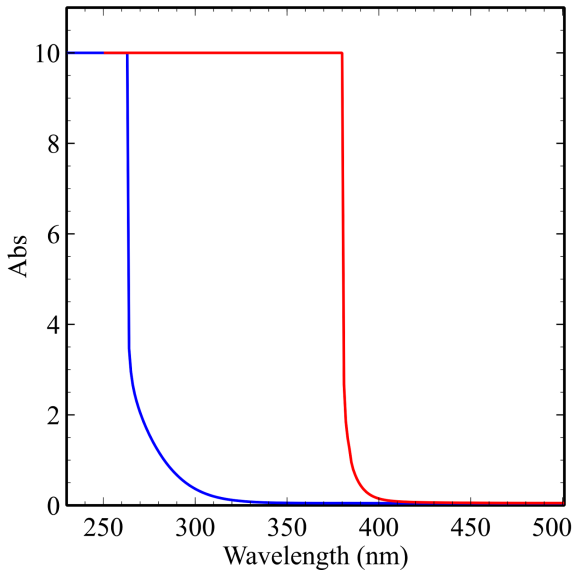

Figure S11 *- Absorption spectra of the borosilicate filter (blue) and of the UV filter (red).*

3 - Experiments carried out with a halogen lamp

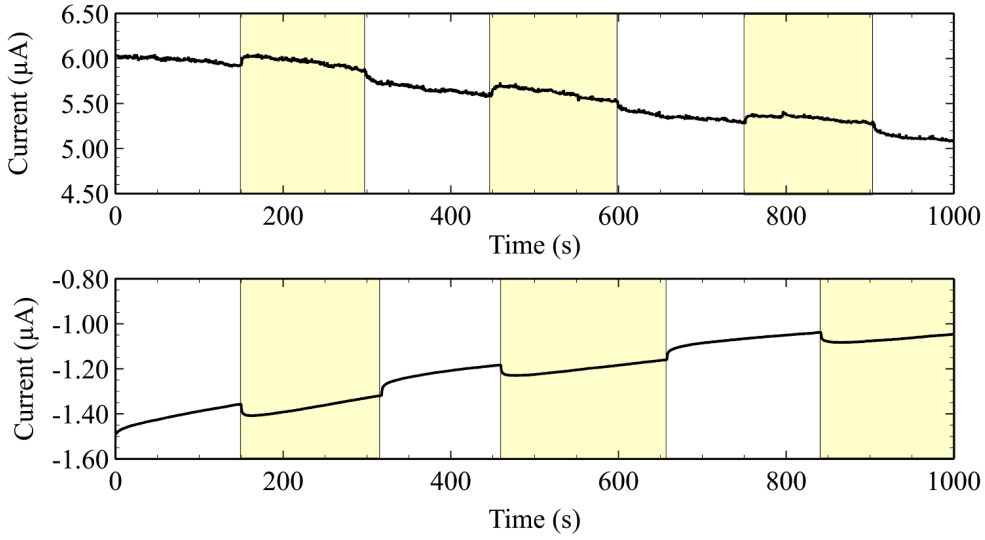

Figure S12 - *Chronoamperogram recorded at 30°C, 1 bar H_2, pH 7, 3 krpm, with C. reinhardtii HydA1 adsorbed on PGE.*

We tested on *C. reinhardtii* the effect of illumination with a halogen lamp. Figure S10 shows that both at -0.158 mV (top panel) and -0.508 mV potential (bottom panel), the current slightly increases when the illumination starts and then it stabilizes (same decay as in the dark, resulting from film loss). When the irradiation is switched off the current decreases and stabilizes. (This is the same observation as the SI of ref [19]).

4 - Photoinhibition time constant values for *C. reinhardtii* and *C. acetobutylicum* FeFe hydrogenases

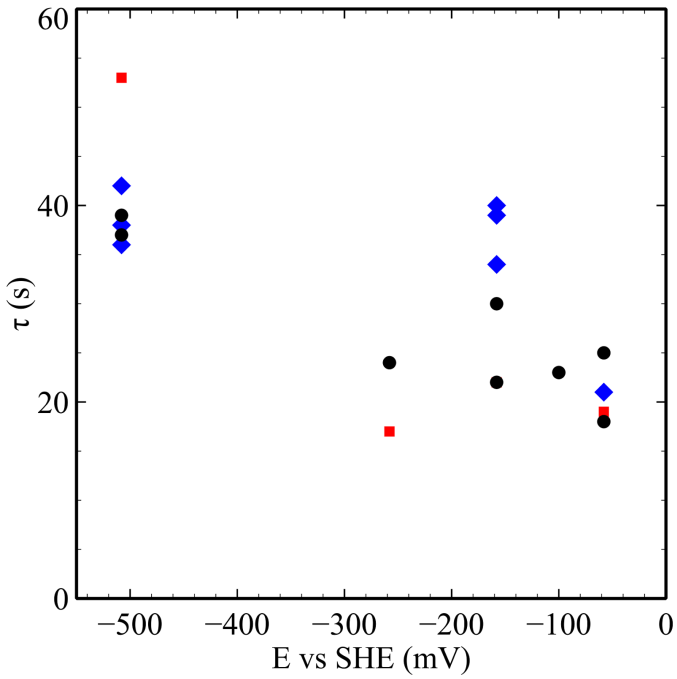

Figure S13 - *Photoinhibition values of τ for C. reinhardtii (blue rhombus) and C. acetobutylicum (black circles) FeFe hydrogenases exposed to 100% H_2 and C. reinhardtii in 10% H_2 (red squares). Conditions: T= 30°C, 3000 rpm, pH 6.8 phosphate buffer.*

5 - *C. acetobutylicum* FeFe hydrogenases inactivation by xenon lamp with or without UV

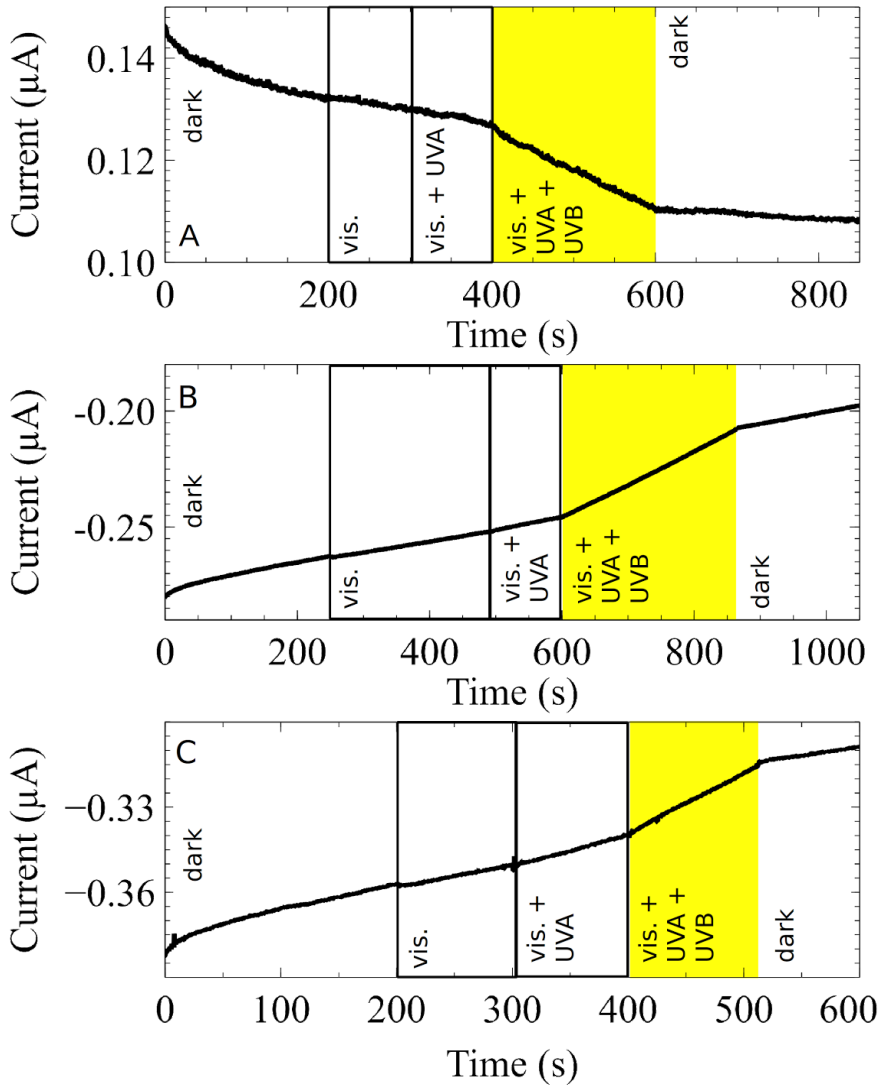

Figure S14 - *Effect of irradiation with a xenon lamp with/without filters. (A) FeFe hydrogenase from C. acetobutylicum at E= -0.158 V and (B) E= -0.508V vs SHE. (C) FeFe hydrogenase from C. reinhardtii E= -0.508V vs SHE. Conditions: T=30°C, 1 bar H_2, pH 6.8, 3 krpm.*

6 - Photo-electrochemical cell

Figure S15 - *Photographs of the photo-electrochemical cell used for the experiments. At the bottom of the cell there is a quartz window. The photographs were taken by the authors.*

References

(1) Nicolet, Y.; Piras, C.; Legrand, P.; Hatchikian, C. E.; Fontecilla-Camps, J. C. *Structure* **1999**, *7*, 13–23.

(2) Cornish, A. J.; Gärtner, K.; Yang, H.; Peters, J. W.; Hegg, E. L. *J. Biol. Chem.* **2011**, *286*, 38341–38347.

(3) Mulder, D. W.; Ratzloff, M. W.; Bruschi, M.; Greco, C.; Koonce, E.; Peters, J. W.; King, P. W. *J. Am. Chem. Soc.* **2014**, *136*, 15394–15402.

(4) Esselborn, J.; Muraki, N.; Klein, K.; Engelbrecht, V.; Metzler-Nolte, N.; Apfel, U.-P.; Hofmann, E.; Kurisu, G.; Happe, T. *Chem. Sci.* **2016**, *7*, 959–968.
(5) Adamo, C.; Scuseria, G. E.; Barone, V. *J. Chem. Phys.* **1999**, *111*, 2889–2899.
(6) Ahlrichs, R.; Bär, M.; Häser, M.; Horn, H.; Kölmel, C. *Chem. Phys. Lett.* **1989**, *162*, 165–169.
(7) Schäfer, A.; Huber, C.; Ahlrichs, R. *J. Chem. Phys.* **1994**, *100*, 5829–5835.
(8) Becke, A. D. *Phys. Rev. A* **1988**, *38*, 3098–3100.
(9) Perdew, J. P. *Phys. Rev. B: Condens. Matter Mater. Phys.* **1986**, *33*, 8822–8824.
(10) Eichkorn, K.; Weigend, F.; Treutler, O.; Ahlrichs, R. *Theor. Chem. Acc.* **1997**, *97* , 119–124.
(11) Siegbahn, P. E. M.; Tye, J. W.; Hall, M. B. *Chem. Rev.* **2007**, *107*, 4414–4435.
(12) Bruschi, M.; Greco, C.; Fantucci, P.; De Gioia, L. *Inorg. Chem.* **2008**, *47*, 6056–6071.
(13) Bertini, L.; Bruschi, M.; de Gioia, L.; Fantucci, P.; Greco, C.; Zampella, G. In *Atomistic Approaches in Modern Biology*; Topics in Current Chemistry; Springer Berlin Heidelberg, 2006; Vol. 268, pp 1–46.
(14) Lee, C.; Yang, W.; Parr, R. G. *Phys. Rev. B: Condens. Matter Mater. Phys.* **1988**, *37*, 785–789.
(15) Zhao, Y.; Truhlar, D. G. *Theor. Chem. Acc.* **2008**, *119*, 525–525.
(16) Tao, J.; Perdew, J. P.; Staroverov, V. N.; Scuseria, G. E. *Phys. Rev. Lett.* **2003**, *91*, 146401.
(17) Staroverov, V. N.; Scuseria, G. E.; Tao, J.; Perdew, J. P. *J. Chem. Phys.* **2003**, *119*, 12129–12137.
(18) Weigend, F.; Ahlrichs, R. *Phys. Chem. Chem. Phys.* **2005**, *7*, 3297–3305.
(19) Goldet, G.; Brandmayr, C.; Stripp, S. T.; Happe, T.; Cavazza, C.; Fontecilla-Camps, J. C.; Armstrong, F. A. *J. Am. Chem. Soc.* **2009**, *131*, 14979–14989.